

Implementation of Traction Constraints in Bragg-edge Neutron Transmission Strain Tomography

J.N. Hendriks^{*1}, A.W.T. Gregg¹, C.M. Wensrich¹, and A. Wills¹

¹*School of Engineering, The University of Newcastle, Callaghan NSW 2308, Australia.*

Abstract

Several recent methods for tomographic reconstruction of stress and strain fields from Bragg-edge neutron strain images have been proposed in the literature. This paper presents an extension of a previously demonstrated approach based on Gaussian Process regression. This extension incorporates knowledge of boundary conditions, primarily boundary tractions, into the reconstruction process. This is shown to increase the rate of convergence and is more tolerant of systematic errors that may be present in experimental measurements. An exact expression for a central calculation in this method is also provided which avoids the need for the approximation scheme that was previously used. Convergence of this method for simulated data is compared to existing approaches and a reconstruction from experimental data is provided. Validation of the results to conventional constant wavelength strain measurements and comparison to prior methods shows a significant improvement.

1 INTRODUCTION

Tomographic reconstruction determines a map of of an unknown quantity within an object from lower dimensional projections. A well known example is Computed Tomography where a set of flat two dimensional X-ray images are analysed to build a three dimensional image of the scalar density. High resolution strain imaging has created significant interest in the associated tomographic reconstruction process. In contrast, tomographic reconstruction of strain seeks to determine the rank-2 tensor strain field from a set of scalar two dimensional projections of the strain field.

Although other approaches exist, energy-resolved neutron transmission has become a prominent method for strain imaging. This technique analyses the relative transmission of a neutron pulse with a known wavelength-intensity spectrum through a sample over an array of detector pixels (Refer to Figure 1). In particular, the relative positions of sudden increases in transmission intensity as a function of wavelength—known as Bragg-edges— can be related to strain.

Bragg-edges are a consequence of coherent scattering; edge positions are related to lattice spacing within the sample through Bragg’s law [1]. In short, neutrons passing through a polycrystalline material can be coherently scattered by crystal planes of a certain spacing until their wavelength corresponds to a scattering

angle of 180° (i.e. backscattering). Above this wavelength no further coherent scattering occurs creating a sudden increase in relative transmission. Multiple Bragg-edges can be found in the transmission spectra corresponding to various lattice spacings within the samples crystal structure [2, 1]. In particular, the relative shift in associated wavelength can be used to measure strain of the form;

$$\langle \epsilon \rangle = \frac{\lambda - \lambda_0}{\lambda_0} \quad (1)$$

where $\langle \epsilon \rangle$ is the normal strain in the transmission direction averaged over the irradiated volume, λ is the measured wavelength of the Bragg-edge, and λ_0 is the same wavelength in an unstressed sample. As with all diffraction techniques, strain measured in this manner refers only to the elastic component.

The relationship between strain measured at each pixel and the strain field within the sample can be modelled by the Longitudinal Ray Transform (LRT) [3];

$$I_\epsilon(\boldsymbol{\eta}) = \frac{1}{L} \int_0^L \hat{\mathbf{n}}^T \boldsymbol{\epsilon}(\mathbf{x}^0 + \hat{\mathbf{n}}s) \hat{\mathbf{n}} ds, \quad (2)$$

where $\boldsymbol{\eta} = \{\hat{\mathbf{n}}, \mathbf{x}^0\}$. This maps the rank-2 tensor strain field $\boldsymbol{\epsilon}$ to the average normal component of strain, $I_\epsilon \in \mathbb{R}$, along the ray with direction $\hat{\mathbf{n}} \in \mathbb{R}^3$, entering the sample at $\mathbf{x}^0 \in \mathbb{R}^3$ and with irradiation length $L \in \mathbb{R}$, see Figure 1.

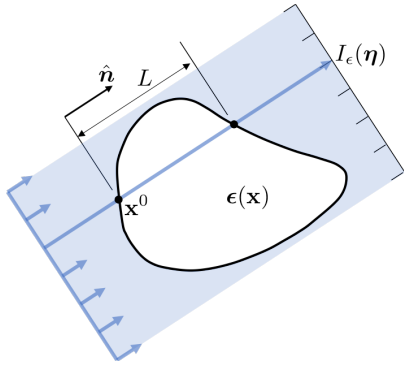


Figure 1: Coordinate system and geometry for the LRT. Each pixel of a strain image provides a measurement of the through thickness average normal strain in the direction of the ray, $I_\epsilon(\boldsymbol{\eta})$.

Inversion of the LRT is the heart of the strain tomographic reconstruction problem. The LRT is a non-injective mapping [3]; strain fields resulting in a set of strain images are not unique. Therefore, additional information is required in order to isolate the correct (physical) strain field from all possibilities. Previous work has considered the inclusion of compatibility and equilibrium constraints (e.g. see [4] and [5]).

Compatibility was assumed in prior work focussing on special cases [6, 7, 8, 4, 9]. Axisymmetric systems were explored in [6, 7], where various basis functions were used to reconstruct strain within quenched cylinders and standard VAMAS ring-and-plug system. Outside of axisymmetric systems, [8] assumed compatibility in a granular system to uniquely relate the average strain within each granule to the measurements. In [4] an algorithm was developed for the reconstruction of a planar strain problem subject to *in-situ* loading and then demonstrated on experimental data in [9]. Here, the assumption of compatibility was used to uniquely relate the boundary deformations to the internal strain field, allowing for the reconstruction of the exclusively elastic strain field.

While compatibility cannot always be assumed, equilibrium is always satisfied in physical systems. Equilibrium was initially used to develop two separate algorithms for axisymmetric systems [10, 11]. In [10] equilibrium was imposed through boundary conditions. In contrast, [11] satisfied equilibrium by minimising strain energy.

More general methods suitable for reconstructing planar residual strain fields have been presented in [12] and [5]—both cases enforce equilibrium. In [12] a finite series of basis functions were fit to the measurements and equilibrium was enforced at a grid

of points through constraints placed on the function derivatives. Whereas, in [5] the strain field is reconstructed with a probabilistic non-parametric approach—Gaussian Process (GP) regression—where equilibrium is enforced over the entire field by relating the strains to Airy’s stress functions, and an appropriate approximation method was used to avoid numerical evaluation of a double line integral.

Conceptually both [12] and [5] reconstruct the strain field by fitting functions. The differences lie in how this is achieved; a GP based method has the potential for greater expressiveness as it is not limited to a finite set of basis functions. However, this advantage is somewhat reduced by the use of an approximation method.

In this paper, we extend the method presented in [5] to incorporate knowledge of the tractions at the samples boundaries, this is demonstrated not only to improve the reconstruction near the boundary but over the entire field. Further, we provide an alternate solution to the problem of numerical integration which avoids the need for the approximation method. Finally, a convergence comparison of the methods given in [4], [12], [5], and the extended method is presented for the reconstruction of the Saint-Venant approximate cantilevered beam strain field [13].

2 METHOD

The focus of this work is on the reconstruction of a strain field given a set of Bragg-edge strain images, where each pixel represents a measurement of the form (2). Details on the measurement of strain images can be found in [1]. We extend the Gaussian process regression method presented in [5] to utilise knowledge of boundary tractions. Salient points of the method are summarised as:

1. Gaussian process regression provides a non-parametric method for fitting functions to data and a revision is provided in Section 2.1.
2. A suitable Gaussian process prior is selected for the strain field ensuring that only functions satisfying equilibrium are contained in the distribution, Section 2.2.
3. The joint distribution between the measurements and the strain field is determined, Section 2.3
4. The joint distribution is extended to include traction constraints, Section 2.4.

5. Estimates of the strain field are given by conditioning the Gaussian process prior on the known tractions and measurements.

2.1 GAUSSIAN PROCESS REGRESSION

A Gaussian process is a stochastic process suitable for modelling spatially correlated functions. The GP is a generalisation of the multivariate Gaussian probability distribution and to a Gaussian distribution over functions. This distribution is uniquely defined over the spatial coordinate \mathbf{x} by a mean function $\mathbf{m}(\mathbf{x}) = \mathbb{E}[\mathbf{f}(\mathbf{x})]$ and a covariance function $\mathbf{K}(\mathbf{x}, \mathbf{x}') = \mathbb{E}[(\mathbf{f}(\mathbf{x}) - \mathbf{m}(\mathbf{x}))(\mathbf{f}(\mathbf{x}') - \mathbf{m}(\mathbf{x}'))^T]$, where \mathbb{E} refers to the expected value.

For example, we can define the distribution of a scalar function to consist of a finite series of polynomial basis functions $f(x) = \phi(x)^T \mathbf{w}$, where $\phi(\mathbf{x}) = (1, x, x^2, \dots, x^n)^T$ and the weights have a prior distribution $\mathbf{w} \sim \mathcal{N}(\mathbf{0}, \Sigma_p)^1$. In this case the GP will have a mean and covariance function given by

$$\begin{aligned} \mathbf{m}(x) &= \phi(x)^T \mathbb{E}[\mathbf{w}] = 0, \\ \mathbf{K}(x, x') &= \phi(x)^T \mathbb{E}[\mathbf{w}\mathbf{w}^T] \phi(x') = \phi(x)^T \Sigma_p \phi(x'). \end{aligned} \quad (3)$$

Here, the covariance function is given by the outer product of a set of basis functions. More generally any function that generates a positive definite symmetric covariance can be used. A common choice is the squared-exponential $K(\mathbf{x}, \mathbf{x}') = \sigma_f^2 \exp(-\frac{1}{2}|\mathbf{x} - \mathbf{x}'|^2)$, this corresponds to a Bayesian linear regression model with an infinite number of basis functions [14].

Gaussian process regression refers to the estimation of function values at specified inputs given a set of measurements—where the measurements can be expressed as linear functionals of the form, $\mathbf{y} = \mathcal{V}_{\mathbf{x}}[\mathbf{f}(\mathbf{x})]$, and have zero-mean Gaussian noise of standard deviation σ_n . A finite set of measurements, $\mathbf{Y} = \{\mathbf{y}_1, \dots, \mathbf{y}_N\}$, for inputs $\mathbf{x}_1, \dots, \mathbf{x}_N$ and the function value evaluated at \mathbf{x}_* are jointly Gaussian;

$$\begin{bmatrix} \mathbf{y}_1 \\ \vdots \\ \mathbf{y}_N \\ \mathbf{f}(\mathbf{x}_*) \end{bmatrix} \sim \mathcal{N} \left(\begin{bmatrix} \boldsymbol{\mu}_y \\ \mathbf{m}(\mathbf{x}_*) \end{bmatrix}, \begin{bmatrix} \mathbf{K}_{yy'} + \sigma_n^2 I & \mathbf{K}_{y*} \\ \mathbf{K}_{y*}^T & \mathbf{K}(\mathbf{x}_*, \mathbf{x}_*) \end{bmatrix} \right)$$

¹The notation, $\mathbf{v} \sim \mathcal{N}(\boldsymbol{\mu}, \Sigma)$ indicates that the vector \mathbf{v} is a normally distributed random variable with mean $\boldsymbol{\mu}$ and variance Σ .

where

$$\boldsymbol{\mu} = \begin{bmatrix} \mathcal{V}_{\mathbf{x}_1} \mathbf{m}(\mathbf{x}_1) \\ \vdots \\ \mathcal{V}_{\mathbf{x}_N} \mathbf{m}(\mathbf{x}_N) \end{bmatrix}, \quad \mathbf{K}_{y*} = \begin{bmatrix} \mathcal{V}_{\mathbf{x}_1} \mathbf{K}(\mathbf{x}_1, \mathbf{x}_*) \\ \vdots \\ \mathcal{V}_{\mathbf{x}_N} \mathbf{K}(\mathbf{x}_N, \mathbf{x}_*) \end{bmatrix}$$

and

$$\mathbf{K}_{yy'} = \begin{bmatrix} \mathcal{V}_{\mathbf{x}_1} \mathbf{K}(\mathbf{x}_1, \mathbf{x}_1) \mathcal{V}_{\mathbf{x}_1}^T & \cdots & \mathcal{V}_{\mathbf{x}_1} \mathbf{K}(\mathbf{x}_1, \mathbf{x}_N) \mathcal{V}_{\mathbf{x}_N}^T \\ \vdots & \ddots & \vdots \\ \mathcal{V}_{\mathbf{x}_N} \mathbf{K}(\mathbf{x}_N, \mathbf{x}_1) \mathcal{V}_{\mathbf{x}_1}^T & \cdots & \mathcal{V}_{\mathbf{x}_N} \mathbf{K}(\mathbf{x}_N, \mathbf{x}_N) \mathcal{V}_{\mathbf{x}_N}^T \end{bmatrix}$$

An estimate, $\boldsymbol{\mu}_{\mathbf{f}_*|\mathbf{Y}}$ of $\mathbf{f}(\mathbf{x}_*)$ and its variance, $\Sigma_{\mathbf{f}_*|\mathbf{Y}}$ based on the measurements is given by;

$$\begin{aligned} \boldsymbol{\mu}_{\mathbf{f}_*|\mathbf{Y}} &= \mathbf{m}(\mathbf{x}_*) + \mathbf{K}_{y*}^T (\mathbf{K}_{yy'} + \sigma_n^2 I)^{-1} (\mathbf{Y} - \boldsymbol{\mu}_y), \\ \Sigma_{\mathbf{f}_*|\mathbf{Y}} &= \mathbf{K}(\mathbf{x}_*, \mathbf{x}_*) - \mathbf{K}_{y*}^T (\mathbf{K}_{yy'} + \sigma_n^2 I)^{-1} \mathbf{K}_{y*}. \end{aligned} \quad (4)$$

Conceptually, if we were to estimate values of an unknown scalar functions using GP regression with mean and covariance function given by (3), then we could think of this as fitting a finite series of polynomials to the measurements. For a more in-depth discussion on GPs see [14].

2.2 STRAIN FIELD GAUSSIAN PROCESS

In this section we design a Gaussian process for strain with mean and covariance function so that the distribution only spans functions that satisfy equilibrium. This means any function values estimated using this GP will automatically satisfy equilibrium. This is done by following the procedure outlined in [5].

We define a GP for a distribution of Airy's Stress functions, $\varphi(\mathbf{x})$, from which we can define stress as $\sigma_{xx}(\mathbf{x}) = \frac{\partial^2 \varphi(\mathbf{x})}{\partial y^2}$, $\sigma_{yy}(\mathbf{x}) = \frac{\partial^2 \varphi(\mathbf{x})}{\partial x^2}$, and $\sigma_{xy}(\mathbf{x}) = \frac{\partial^2 \varphi(\mathbf{x})}{\partial x \partial y}$. From Hooke's law, under an assumption of plane stress, this provides strain of;

$$\boldsymbol{\mathcal{E}}(\mathbf{x}) = \underbrace{\begin{bmatrix} \frac{\partial^2}{\partial y^2} - \nu \frac{\partial^2}{\partial x^2} \\ (1 + \nu) \frac{\partial^2}{\partial x \partial y} \\ \frac{\partial^2}{\partial x^2} - \nu \frac{\partial^2}{\partial y^2} \end{bmatrix}}_{\mathcal{L}_{\mathbf{x}}} \psi(\mathbf{x}) = \mathcal{L}_{\mathbf{x}} \varphi(\mathbf{x}), \quad (5)$$

where $\boldsymbol{\mathcal{E}} = [\epsilon_{xx}, \epsilon_{xy}, \epsilon_{yy}]^T$, and ν is poisson's ratio.

The distribution of $\varphi(\mathbf{x})$ is assumed to have mean $m_{\varphi}(\mathbf{x}) = 0$, covariance $K_{\varphi}(\mathbf{x}, \mathbf{x}')$, and $\mathbf{x} = [x, y]^T$. This allows us to write a GP for the strain field with

mean function $\mathbf{m}_\epsilon = \mathcal{L}_\mathbf{x} m_\varphi(\mathbf{x}) = \mathbf{0}$ and covariance function

$$\mathbf{K}_{\epsilon\epsilon}(\mathbf{x}, \mathbf{x}') = \mathcal{L}_\mathbf{x} K_\varphi(\mathbf{x}, \mathbf{x}') \mathcal{L}_\mathbf{x}^T. \quad (6)$$

This is possible as GPs are closed under linear functional transformations [15, 16, 17].

Although many options exist for the choice of covariance function $K_\varphi(\mathbf{x}, \mathbf{x}')$, the squared-exponential and Matern covariance functions were both shown to be suitable in [5]. It is also possible to build a covariance function from the finite two-dimensional Fourier basis used in [12], however we would then be required to specify the number of basis functions used, limiting the expressiveness of the Gaussian process.

The shorthand $K_\varphi = K_\varphi(\mathbf{x}_i, \mathbf{x}_j)$ and $\mathbf{K}_{\epsilon\epsilon} = \mathbf{K}_{\epsilon\epsilon}(\mathbf{x}_i, \mathbf{x}_j)$ will be used where appropriate.

2.3 MEASUREMENT JOINT DISTRIBUTION

In order to estimate the values of the strain field from a set of strain images, we require the joint distribution of the measurements, \mathbf{I}_ϵ , and strains;

$$\begin{bmatrix} \mathbf{I}_\epsilon \\ \boldsymbol{\epsilon} \end{bmatrix} \sim \mathcal{N} \left(\begin{bmatrix} \mathbf{0} \\ \mathbf{0} \end{bmatrix}, \begin{bmatrix} \mathbf{K}_{II} + \sigma_n^2 I & \mathbf{K}_{I\epsilon} \\ \mathbf{K}_{I\epsilon}^T & \mathbf{K}_{\epsilon\epsilon} \end{bmatrix} \right)$$

The cross covariance between an LRT measurement $I_{\epsilon i}$ and strain at the j^{th} input location \mathbf{x}_j is

$$\mathbf{K}_{I\epsilon}(\boldsymbol{\eta}_i, \mathbf{x}_j) = \frac{1}{L_i} \int_0^{L_i} \bar{\mathbf{n}}_i \mathbf{K}_{\epsilon\epsilon}(\mathbf{x}_i^0 + \hat{\mathbf{n}}_i s, \mathbf{x}_j) ds \quad (7)$$

where $\bar{\mathbf{n}} = [\hat{n}_1^2 \quad 2\hat{n}_1\hat{n}_2 \quad \hat{n}_2^2]$. The covariance between two measurements, $I_{\epsilon i}$ and $I_{\epsilon j}$ is given by

$$\mathbf{K}_{II}(\boldsymbol{\eta}_i, \boldsymbol{\eta}_j) = \frac{1}{L_i L_j} \int_0^{L_i} \int_0^{L_j} \bar{\mathbf{n}}_i \mathbf{K}_{\epsilon\epsilon}(\mathbf{x}_i^0 + \hat{\mathbf{n}}_i s, \mathbf{x}_j^0 + \hat{\mathbf{n}}_j s) \bar{\mathbf{n}}_j^T ds_i ds_j.$$

In its current form, an analytical solution to (7) appears intractable and [5] proposed either the use of numerical integration or an approximation scheme. However, in the special cases where the x or y direction of the strain is aligned with the line integral an analytical solution is apparent (i.e. $ds = dx$). This can be used to provide a general solution by noting that strain can be rotated from a coordinate system aligned with the ray to the global coordinate system

according to $\boldsymbol{\epsilon} = \mathbf{R}(\hat{\mathbf{n}}_i) \boldsymbol{\epsilon}^{\{i\}} \mathbf{R}(\hat{\mathbf{n}}_i)^T$, where $\boldsymbol{\epsilon}^{\{i\}}$ is defined as strain expressed in the coordinates of line i and

$$\mathbf{R}(\hat{\mathbf{n}}_i) = \begin{bmatrix} \hat{n}_1 & -\hat{n}_2 \\ \hat{n}_2 & \hat{n}_1 \end{bmatrix}.$$

In vector form this can be written as

$$\boldsymbol{\epsilon} = \underbrace{\begin{bmatrix} \hat{n}_1^2 & -2\hat{n}_1\hat{n}_2 & \hat{n}_2^2 \\ \hat{n}_2\hat{n}_1 & \hat{n}_1^2 - \hat{n}_2^2 & -\hat{n}_1\hat{n}_2 \\ \hat{n}_2^2 & 2\hat{n}_1\hat{n}_2 & \hat{n}_1^2 \end{bmatrix}}_{\mathbf{J}(\hat{\mathbf{n}}_i)} \boldsymbol{\epsilon}^{\{i\}}$$

Therefore, the covariance can now be written as

$$\mathbf{K}_{I\epsilon}(\boldsymbol{\eta}_i, \mathbf{x}_j) = \frac{1}{L_i} \bar{\mathbf{n}}^{\{i\}} \mathcal{V}_{\mathbf{x}_i} K_\varphi \mathcal{L}_{\mathbf{x}_j}^T \mathbf{J}(\hat{\mathbf{n}}_i)^T, \quad (8)$$

$$\mathcal{V}_{\mathbf{x}_i} = \begin{bmatrix} \int_0^{L_i} \frac{\partial^2}{\partial y_i^2} dx_i - \nu \frac{\partial}{\partial x_i} \\ (1 + \nu) \frac{\partial}{\partial y_i} \\ \frac{\partial}{\partial x_i} - \nu \int_0^{L_i} \frac{\partial^2}{\partial y_i^2} dx_i \end{bmatrix}.$$

Here, $\bar{\mathbf{n}}^{\{i\}} = [1, 0, 0]$. The solutions to these equations are given in Appendix A.

Unfortunately, the same technique used to solve the first integral cannot be applied to the second integral as the strain cannot be simultaneously expressed in two different coordinate systems. However, using (8) we are required to only numerically evaluate a single integral—improving computation time and accuracy.

Extension to non-convex geometry is straightforward; the measurement model becomes a sum of integrals over each segment. Details can be found in [5].

2.4 BOUNDARY TRACTIONS

So far, we have a joint distribution that allows the estimation of strains satisfying equilibrium from Bragg-edge neutron strain measurements. The estimation of these strains can be improved by including knowledge about tractions acting on the surface. Strain within a physical body is subject to conditions imposed upon it by the tractions on its surface. Firstly, tractions can be directly related to stress at the surface and hence to strain using

$$T_i = C_{ijkl} \epsilon_{kl} n_j,$$

where \mathbf{C} is the stiffness tensor from Hooke's law that relates strain to stress, and \mathbf{n} is the surface normal.

Secondly, knowledge of the boundary tractions can inform us about the average stress (hence strain) within

a solid. The mean stress theorem [18] states that when equilibrium is satisfied, and in the absence of body forces, the average stress within a body, \mathcal{B} , is related to the surface integral of the tractions through

$$\frac{1}{V} \int_{\mathcal{B}} \boldsymbol{\sigma}(\mathbf{x}) dv = \frac{1}{2V} \int_{\partial \mathcal{B}} (\mathbf{x} \otimes \mathbf{T}(\mathbf{x}) + \mathbf{T}(\mathbf{x}) \otimes \mathbf{x}) da.$$

While we are unlikely to know the distribution of surface tractions at a point of loading, surface areas not subject to contact loads will have zero-tractions. This is particularly applicable to residual strain problems where there are often no surface tractions at all. This knowledge is incorporated into the reconstruction process by the inclusion of artificial zero strain observations. Assuming plane stress, these observations are related to our strain function by

$$\mathbf{T} = \underbrace{\begin{bmatrix} n_1 & n_2 & 0 \\ 0 & n_1 & n_2 \end{bmatrix}}_{\tilde{\mathbf{n}}} \underbrace{\frac{E}{1-\nu^2} \begin{bmatrix} 1 & 0 & \nu \\ 0 & 1-\nu & 0 \\ \nu & 0 & 1 \end{bmatrix}}_{\mathbf{C}_{2D}} \boldsymbol{\varepsilon}.$$

The covariance between traction observations, the cross covariance between traction observations and strains, and the cross covariance between LRT measurements and traction observations are given by

$$\begin{aligned} \mathbf{K}_{TT}(\mathbf{x}_i, \mathbf{x}_j) &= \tilde{\mathbf{n}} \mathbf{C}_{2D} \mathbf{K}_{\epsilon\epsilon}(\mathbf{x}_i, \mathbf{x}_j) \mathbf{C}_{2D}^T \tilde{\mathbf{n}}^T \\ \mathbf{K}_{T\epsilon}(\mathbf{x}_i, \mathbf{x}_j) &= \tilde{\mathbf{n}} \mathbf{C}_{2D} \mathbf{K}_{\epsilon\epsilon}(\mathbf{x}_i, \mathbf{x}_j) \\ \mathbf{K}_{IT} &= \mathbf{K}_{I\epsilon}(\boldsymbol{\eta}_i, \mathbf{x}_j) \mathbf{C}_{2D}^T \tilde{\mathbf{n}} \end{aligned}$$

The joint distribution of the strains, LRT measurements, and the zero-traction observations is then given by

$$\begin{bmatrix} \mathbf{I}_{\epsilon} \\ \mathbf{T} \\ \boldsymbol{\varepsilon} \end{bmatrix} \sim \mathcal{N} \left(\begin{bmatrix} \mathbf{0} \\ \mathbf{0} \\ \mathbf{0} \end{bmatrix}, \begin{bmatrix} \mathbf{K}_{II} + \sigma_n^2 \mathbf{I} & \mathbf{K}_{IT} & \mathbf{K}_{I\epsilon} \\ \mathbf{K}_{IT}^T & \mathbf{K}_{TT} & \mathbf{K}_{T\epsilon} \\ \mathbf{K}_{I\epsilon}^T & \mathbf{K}_{T\epsilon}^T & \mathbf{K}_{\epsilon\epsilon} \end{bmatrix} \right)$$

Strain estimates can now be made using both measurements from strain images and knowledge of the boundary tractions.

3 DEMONSTRATION— SIMULATION

Reconstructing the strain field of the classical cantilevered beam has been examined in [4, 5] and [12]. As such, we use this example to demonstrate the improvement that incorporating boundary tractions has on the reconstruction. A direct comparison of the

convergence of these methods as well as a Gaussian process method that includes boundary tractions is provided.

The classical cantilevered beam is shown in Figure 2 and the Saint-Venant approximation [13] to the strain field is:

$$\boldsymbol{\varepsilon}(\mathbf{x}) = \begin{bmatrix} \frac{P}{EI}(L-x)y \\ -\frac{(1+\nu)P}{2EI} \left(\left(\frac{h}{2} \right)^2 - y^2 \right) \\ -\frac{\nu P}{EI}(L-x)y \end{bmatrix} \quad (9)$$

Strain images were numerically simulated from this field assuming 512 pixels per projection and a detector width of 28mm (corresponding to Micro-Channel Plate (MCP) detector specifications currently used in experiments [19]). The values at each pixel correspond to a measurement of the form (2) and were corrupted with zero-mean Gaussian noise of standard deviation $\sigma = 1.25e - 4$.

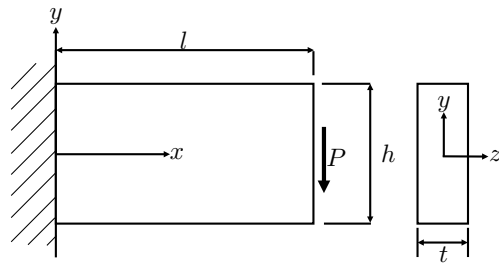


Figure 2: Cantilever beam geometry and coordinate system with $l = 20\text{mm}$, $h = 10\text{mm}$, $t = 5\text{mm}$, $E = 200\text{GPa}$, $P = 2\text{kN}$, $\nu = 0.3$, and $I = \frac{th^3}{12}$.

To demonstrate the benefit of including boundary tractions, reconstruction of the strain field from a limited set of measurements was performed with and without the inclusion of tractions (Figure 3). The subset of measurements consists of 40 pixels from each of 4 different projections. Without the inclusion of boundary tractions the reconstruction shows significant error, particularly the ϵ_{xy} component. Zero-traction measurements were then included at 100 points along the top and bottom surface of the cantilevered beam (where it is known to have zero-traction), and the subsequent reconstruction shows considerable improvement.

Convergence of the algorithm is shown in Figure 4 and compared to the boundary reconstruction method [4], a finite basis method [12] with $n = 6$ wave numbers, and a Gaussian process method that does not include traction measurements [5]. For each reconstruction, projection angles were evenly spaced over 180° degrees. Both Gaussian process regression methods

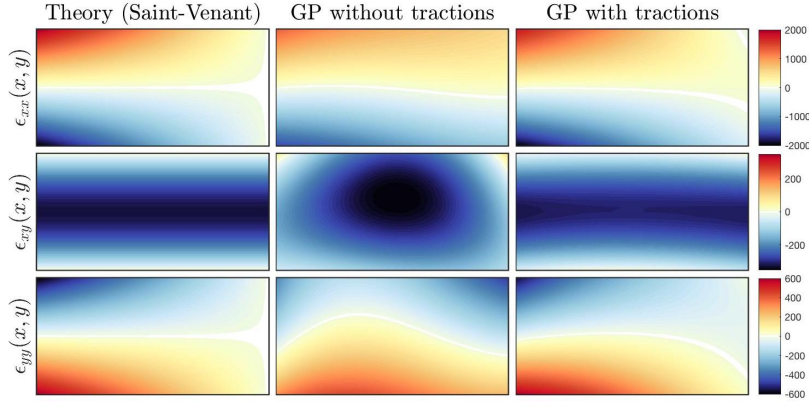


Figure 3: (Left) The Saint-Venant strain field from which measurements were generated. (Center) Reconstruction from a limited measurement set using the Gaussian process method presented in [5]. (Right) Reconstruction from a limited measurement set using the Gaussian process method extended to include boundary tractions.

show significantly faster convergence than the other algorithms, with the inclusion of tractions converging fastest with less than 5% relative error for three projections—the minimum number of unique projections angles required in two dimensions [4]. For 51 projections the methods excluding the boundary reconstruction approach show good convergence to the theoretical solution. With the current algorithm giving a marginally better relative error of 0.9% compared to 1.05% and 1.15% for the methods from [5] and [12], respectively.

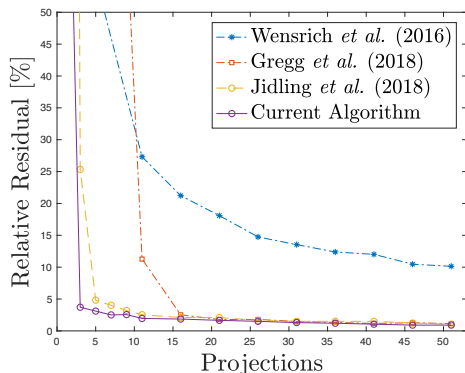


Figure 4: The convergence of the current algorithm compared to the boundary reconstruction method [4], the finite basis method [12], and the Gaussian process regression method demonstrated in [5].

4 EXPERIMENTAL RESULTS

The extended method has been applied to data from an experiment on the RADEN (Energy Resolved Neutron Imaging) instrument at the Japan Proton Accelerator Research Complex (J-PARC) [20, 21] in January 2018. Strain images were taken from the residual strain field within an EN26 steel crushed ring formed by plastically deforming a hollow cylinder. This sample was initially heat treated to relieve residual stress, giving a final hardness of 290HV. It was then plastically deformed by 1.5mm, as shown in Figure 5, using approximately 8.4kN of load. Data collection and processing of the Bragg-edges is described in [12], with a total of 20,664 measurements of the form (2) collected over 50 projections.

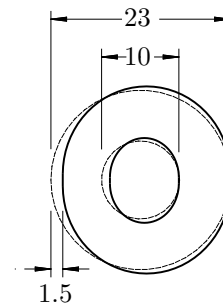


Figure 5: Crushed ring sample geometry. Dimensions are in mm.

The strain field reconstructed from these measurements is shown in Figure 6. Zero-traction measurements are included at 200 points on both the interior and exterior boundary. The result is compared to de-

tailed conventional strain scans [22, 23, 24] from the KOWARI constant wavelength strain-diffractometer at the Australian Nuclear Science and Technology Organisation (ANSTO) [25, 26, 27]. These scans provide measurements of the three in-plane components of strain over a mesh of points within the sample using a 0.5×0.5 mm gauge volume. Details of these measurements can be found in [12].

Comparison to the KOWARI strain scans shows close agreement, with a clear reduction in error compared to reconstructions using prior methods [5, 12]. In particular, the banding in the ϵ_{xx} component has been reduced in-line with the KOWARI results, and concentrations in the ϵ_{yy} component have been reduced and captures more of the square shaped tensile region present in the KOWARI results. Although greatly reduced, some error still exists, particularly in the ϵ_{xy} component for which the magnitude is slightly reduced away from the sample boundary. It should be noted that the KOWARI strain fields are interpolated (and extrapolated on the boundaries) from a grid of point-wise measurements; these interpolations may not satisfy equilibrium or the condition of zero boundary tractions. Hence, the KOWARI strain fields should not be treated as absolute ground truth but rather as a good validation.

Reconstructions, using all illustrated methods, from measurements simulated using the LRT through the interpolated KOWARI strain maps do not display these errors. This suggests the error is not caused by the particular field or sample geometry, but rather by systematic errors in the Bragg-edge fitting. Potential sources of these errors are discussed in detail in [12], and are summarised as: a thickness-dependent shift in edge-centres, possibly due to beam hardening [28], resulting in pseudostrains present in the measurements; complications in the edge fitting process due to strain gradients; and the combined effects of beam divergence and potential sample misalignment. The impact of these systematic errors on the reconstruction has been reduced by including knowledge of the boundary tractions into the algorithm. Correction of these systematic errors is an area of continued research.

5 CONCLUSION AND FUTURE WORK

A method for incorporating known boundary tractions into an algorithm suitable for reconstructing two-dimensional strain fields from Bragg-edge neu-

tron strain images has been presented. The inclusion of boundary tractions reduces the number of measurements required and improves the algorithms ability to reject noise; in particular, systematic noise. This method ensures that the entire field satisfies equilibrium and is therefore suitable for reconstructing residual strain fields.

Additionally, an analytical solution is provided to the first integral of the measurement covariance. This eliminates the need to approximate the GP by a finite set of basis functions, removing the need to choose the number of basis functions and maintaining a greater expressiveness.

This method was demonstrated in simulation, where the inclusion of boundary tractions was shown to significantly improve the result when a limited measurement set was used. Further, a convergence comparison was provided highlighting the benefit of a Gaussian process based method over other available approaches with a GP method including boundary tractions converging fastest.

Results from a reconstruction of a residual strain field within a crushed ring from experimental data collected on the RADEN energy resolved neutron imaging instrument were presented. These results showed closer agreement with strain scans measured using the KOWARI constant wavelength diffractometer when compared with the previous method. This reduction in error demonstrates that the inclusion of boundary tractions reduces the impact of systematic measurement error.

Future work will focus on extending the Gaussian process regression method to three-dimensions. Although Airy's stress functions can only be used to represent two-dimensional fields, the Beltrami stress functions are a suitable alternative. Whereas it is not possible to show that every strain field can be written as a combination of Airy's stress functions, the Beltrami stress functions provide a complete solution to the equilibrium equations [29]. The method presented for including traction constraints can be trivially extended to three-dimensions. Additionally, the inclusion of boundary tractions could be used ensure equilibrium is satisfied at contact points between multiple bodies.

6 ACKNOWLEDGEMENTS

This work is supported by the Australian Research Council through a Discovery Project Grant (DP170102324). Access to the RADEN and

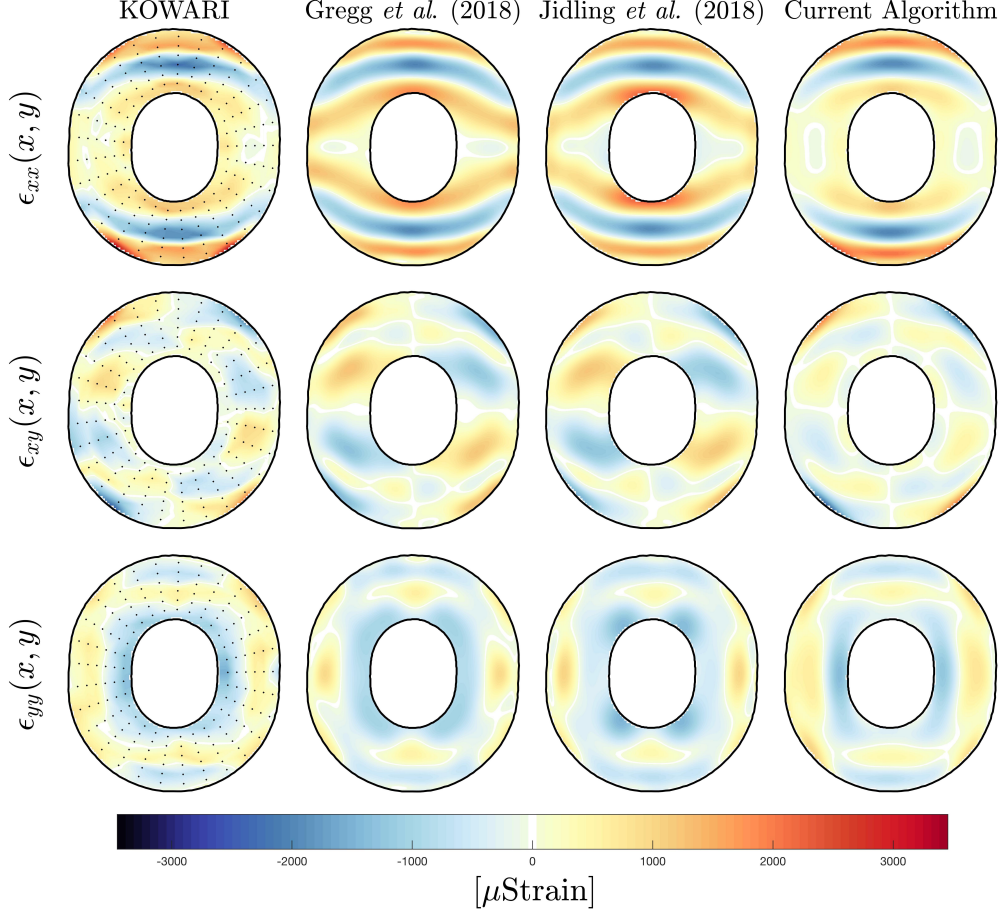


Figure 6: (Left) Strain fields interpolated from point-wise KOWARI strain scans (markers indicate measurement locations) compared to reconstructions from strain images taken using RADEN. (Center left) reconstruction presented in Gregg *et al.* (2018) [12]. (Center right) Reconstruction using the method presented in Jidling *et al.* (2018)[5]. (Right) Current Algorithm that includes boundary tractions.

KOWARI instruments was made possible through the respective user access programs of J-PARC and ANSTO (J-PARC Long Term Proposal 2017L0101 and ANSTO Program Proposal PP6050). The authors would also like to thank AINSE Limited for providing financial assistance (PGRA) and support to enable work on this project.

Where

$$\begin{aligned} \Gamma_1 &= \nu^2 \left[\frac{\partial^3}{\partial x_i \partial x_j^2} K_\psi \right]_0^{L_i} - 2\nu \left[\frac{\partial^3}{\partial x_i \partial y_j^2} K_\psi \right]_0^{L_i} \\ &\quad + \int_0^L \frac{\partial^4}{\partial y_i^2 \partial y_j^2} K_\psi dx_i, \\ \Gamma_2 &= -\nu(\nu + 1) \left[\frac{\partial^3}{\partial y_i \partial x_j^2} K_\psi \right]_0^{L_i} \\ &\quad + (\nu + 1) \left[\frac{\partial^3}{\partial y_i \partial y_j^2} K_\psi \right]_0^{L_i}, \\ \Gamma_3 &= -\nu \left[\frac{\partial^3}{\partial x_i \partial x_j^2} K_\psi \right]_0^{L_i} + (1 + \nu^2) \left[\frac{\partial^3}{\partial x_i \partial y_j^2} K_\psi \right]_0^{L_i} \\ &\quad - \nu \int_0^{L_i} \frac{\partial^4}{\partial y_i^2 \partial y_j^2} K_\psi dx_i. \end{aligned}$$

A Line Integral Equations

Expanding the terms given in (8) yields

$$\mathbf{K}_{I\epsilon}(\boldsymbol{\eta}_i, \mathbf{x}_j) = \frac{1}{L_i} [\Gamma_1 \quad \Gamma_2 \quad \Gamma_3] \mathbf{J}(\hat{\mathbf{n}}_i)^T$$

Here, we have used the fact that $\frac{\partial}{\partial y_i \partial x_j} = \frac{\partial}{\partial x_i \partial y_j}$.

If the covariance function $K_\psi(\mathbf{x}_i, \mathbf{x}_j)$ is chosen to be the squared-exponential then;

$$\frac{\partial^3}{\partial x_i \partial x_j^2} K_\psi = \frac{3}{l_1^4} (x_i - x_j) K_\psi - \frac{1}{l_1^6} (x_i - x_j)^3 K_\psi,$$

$$\begin{aligned} \frac{\partial^3}{\partial x_i \partial y_j^2} K_\psi &= \frac{1}{l_1^2 l_2^2} (x_i - x_j) K_\psi \\ &\quad - \frac{1}{l_1^4 l_2^4} (x_i - x_j) (y_i - y_j)^2 K_\psi, \end{aligned}$$

$$\frac{\partial^3}{\partial y_i \partial y_j^2} K_\psi = \frac{3}{l_2^4} (y_i - y_j) K_\psi - \frac{1}{l_2^6} (y_i - y_j)^3 K_\psi,$$

$$\begin{aligned} \frac{\partial^3}{\partial y_i \partial x_j^2} K_\psi &= \frac{1}{l_1^2 l_2^2} (y_i - y_j) K_\psi \\ &\quad - \frac{1}{l_1^4 l_2^2} (x_i - x_j)^2 (y_i - y_j) K_\psi, \end{aligned}$$

$$\int_0^{L_i} \frac{\partial^4}{\partial y_i^2 \partial y_j^2} K_\psi dx_i = C_y \int_0^{L_i} K_\psi dx_i$$

$$C_y = \left(\frac{1}{l_2^8} (y_i - y_j)^4 - \frac{6}{l_2^6} (y_i - y_j)^2 + \frac{3}{l_2^4} \right)$$

$$\int_0^{L_i} K_\psi dx_i = \left[-\sigma_f^2 \sqrt{\frac{\pi}{2}} l_1 \exp\left(\frac{-(y_i - y_j)^2}{2l_2^2}\right) \right. \\ \left. \operatorname{erf}\left(\frac{x_j - x_i}{\sqrt{2}l_1}\right) \right]_0^{L_i}$$

References

- [1] J. Santisteban, L. Edwards, M. Fitzpatrick, A. Steuwer, and P. Withers, "Engineering applications of bragg-edge neutron transmission," *Applied Physics A*, vol. 74, no. 1, pp. s1433–s1436, 2002.
- [2] J. Santisteban, L. Edwards, M. Fitzpatrick, A. Steuwer, P. Withers, M. Daymond, M. Johnson, N. Rhodes, and E. Schooneveld, "Strain imaging by bragg edge neutron transmission," *Nuclear Instruments and Methods in Physics Research Section A: Accelerators, Spectrometers, Detectors and Associated Equipment*, vol. 481, no. 1, pp. 765–768, 2002.
- [3] W. R. Lionheart and P. J. Withers, "Diffraction tomography of strain," *Inverse Problems*, vol. 31, no. 4, p. 045005, 2015.
- [4] C. Wensrich, J. Hendriks, A. Gregg, M. Meylan, V. Luzin, and A. Tremsin, "Bragg-edge neutron transmission strain tomography for in situ loadings," *Nuclear Instruments and Methods in Physics Research Section B: Beam Interactions with Materials and Atoms*, vol. 383, pp. 52–58, 2016.
- [5] C. Jidling, J. Hendriks, N. Wahlström, A. Gregg, T. B. Schön, C. Wensrich, and A. Wills, "Probabilistic modelling and reconstruction of strain," *arXiv preprint arXiv:1802.03636*, 2018.
- [6] B. Abbey, S. Y. Zhang, W. J. Vorster, and A. M. Korsunsky, "Feasibility study of neutron strain tomography," *Procedia Engineering*, vol. 1, no. 1, pp. 185–188, 2009.
- [7] B. Abbey, S. Y. Zhang, W. Vorster, and A. M. Korsunsky, "Reconstruction of axisymmetric strain distributions via neutron strain tomography," *Nuclear Instruments and Methods in Physics Research Section B: Beam Interactions with Materials and Atoms*, vol. 270, pp. 28–35, 2012.
- [8] C. Wensrich, J. Hendriks, and M. Meylan, "Bragg edge neutron transmission strain tomography in granular systems," *Strain*, vol. 52, no. 1, pp. 80–87, 2016.
- [9] J. Hendriks, A. Gregg, C. Wensrich, A. Tremsin, T. Shinohara, M. Meylan, E. Kisi, V. Luzin, and O. Kirsten, "Bragg-edge elastic strain tomography for in situ systems from energy-resolved neutron transmission imaging," *arXiv preprint arXiv:1708.03426*, 2017.
- [10] H. J. Kirkwood, S. Y. Zhang, A. S. Tremsin, A. M. Korsunsky, N. Baimpas, and B. Abbey, "Neutron strain tomography using the radon transform," *Materials Today: Proceedings*, vol. 2, pp. S414–S423, 2015.
- [11] A. Gregg, J. Hendriks, C. Wensrich, and M. Meylan, "Tomographic reconstruction of residual strain in axisymmetric systems from bragg-edge neutron imaging," *Mechanics Research Communications*, 2017.
- [12] A. Gregg, J. Hendriks, C. Wensrich, A. Wills, A. Tremsin, V. Luzin, T. Shinohara, O. Kirsten, M. Meylan, and E. Kisi, "Tomographic reconstruction of two-dimensional residual strain fields from bragg-edge neutron imaging," *Physical Review Applied*, submitted February 2018.

- [13] F. Beer, E. Johnston Jr, J. Dewolf, and D. Mazurek, “Mechanics of materials, sixth edit edition,” 2010.
- [14] C. E. Rasmussen and C. K. Williams, *Gaussian processes for machine learning*, vol. 1. MIT press Cambridge, 2006.
- [15] A. Papoulis and S. U. Pillai, *Probability, random variables, and stochastic processes*. Tata McGraw-Hill Education, 2002.
- [16] P. Hennig and M. Kiefel, “Quasi-newton method: A new direction,” *Journal of Machine Learning Research*, vol. 14, no. Mar, pp. 843–865, 2013.
- [17] N. Wahlström, *Modeling of Magnetic Fields and Extended Objects for Localization Applications*. PhD thesis, Linköping University Electronic Press, 2015.
- [18] N. D. Cristescu, E.-M. Craciun, and E. Soós, *Mechanics of elastic composites*. CRC Press, 2003.
- [19] A. Tremsin, J. McPhate, A. Steuwer, W. Kockelmann, A. M Paradowska, J. Kelleher, J. Vallerga, O. Siegmund, and W. Feller, “High-resolution strain mapping through time-of-flight neutron transmission diffraction with a microchannel plate neutron counting detector,” *Strain*, vol. 48, no. 4, pp. 296–305, 2012.
- [20] T. Shinohara and T. Kai, “Commissioning start of energy-resolved neutron imaging system, raden in j-parc,” *Neutron news*, vol. 26, no. 2, pp. 11–14, 2015.
- [21] K. Nakajima, Y. Kawakita, S. Itoh, J. Abe, K. Aizawa, H. Aoki, H. Endo, M. Fujita, K. Funakoshi, W. Gong, *et al.*, “Materials and life science experimental facility (mlf) at the japan proton accelerator research complex ii: Neutron scattering instruments,” *Quantum Beam Science*, vol. 1, no. 3, p. 9, 2017.
- [22] E. H. Kisi and C. J. Howard, *Applications of neutron powder diffraction*, vol. 15. Oxford University Press, 2012.
- [23] M. E. Fitzpatrick and A. Lodini, *Analysis of residual stress by diffraction using neutron and synchrotron radiation*. CRC Press, 2003.
- [24] I. C. Noyan and J. B. Cohen, *Residual stress: measurement by diffraction and interpretation*. Springer, 2013.
- [25] O. Kirstein, V. Luzin, and U. Garbe, “The strain-scanning diffractometer kowari,” *Neutron News*, vol. 20, no. 4, pp. 34–36, 2009.
- [26] A. Brule and O. Kirstein, “Residual stress diffractometer kowari at the australian research reactor opal: status of the project,” *Physica B: Condensed Matter*, vol. 385, pp. 1040–1042, 2006.
- [27] O. Kirstein, U. Garbe, and V. Luzin, “Kowariopal’s new stress diffractometer for the engineering community: Capabilities and first results,” in *Materials Science Forum*, vol. 652, pp. 86–91, Trans Tech Publ, 2010.
- [28] S. Vogel, *A Rietveld-approach for the analysis of neutron time-of-flight transmission data*. PhD thesis, Christian-Albrechts Universität Kiel, 2000.
- [29] M. H. Sadd, *Elasticity: theory, applications, and numerics*. Academic Press, 2009.